JGR Solid Earth

RESEARCH ARTICLE
10.1029/2024JB029102

Special Collection:
Advanced machine learning in solid earth geoscience

DASEventNet: AI-Based Microseismic Detection on Distributed Acoustic Sensing Data From the Utah FORGE Well 16A (78)-32 Hydraulic Stimulation

Pengliang Yu[1,2], Tieyuan Zhu[1,2], Chris Marone[1,2,3], Derek Elsworth[1,2], and Mingzhao Yu[4]

[1]Department of Geosciences, Pennsylvania State University, University Park, PA, USA, [2]EMS Energy Institute, Pennsylvania State University, University Park, PA, USA, [3]Dipartimento di Scienze della Terra, La Sapienza Università di Roma, Roma, Italy, [4]School of Electrical Engineering and Computer Science, Pennsylvania State University, University Park, PA, USA

Key Points:

- Developed DASEventNet model achieves 100% accuracy rate in distinguishing microearthquakes (MEQs) from noise in the raw test data set
- Compared to STA/LTA method, DASEventNet model detected ~5 times more MEQs with minimum detectable magnitude of M_w−1.80
- The distribution of the newly identified MEQs defines an extensive stimulation zone and more accurately characterizes fracture geometry

Supporting Information:

Supporting Information may be found in the online version of this article.

Correspondence to:

P. Yu and T. Zhu,
pmy5077@psu.edu;
tuz47@psu.edu

Citation:

Yu, P., Zhu, T., Marone, C., Elsworth, D., & Yu, M. (2024). DASEventNet: AI-based microseismic detection on distributed acoustic sensing data from the Utah FORGE well 16A (78)-32 hydraulic stimulation. *Journal of Geophysical Research: Solid Earth*, *129*, e2024JB029102. https://doi.org/10.1029/2024JB029102

Received 12 MAR 2024
Accepted 21 AUG 2024

Author Contributions:

Conceptualization: Pengliang Yu, Tieyuan Zhu
Funding acquisition: Chris Marone, Derek Elsworth
Investigation: Pengliang Yu, Tieyuan Zhu
Methodology: Pengliang Yu

Abstract Distributed acoustic sensing (DAS) has emerged as a promising seismic technology for monitoring microearthquakes (MEQs) with high spatial resolution. Efficient algorithms are needed for processing large DAS data volumes. This study introduces a deep learning (DL) model based on a Residual Convolutional Neural Network (ResNet) for detecting MEQs using DAS data, named as DASEventNet. The test data were collected from the Utah FORGE 16A (78)-32 hydraulic stimulation experiments conducted in April 2022. The DASEventNet model achieves a remarkable accuracy of 100% when discriminating MEQs from noise in the raw test set of 260 examples. Surprisingly, the model identified weak MEQ signatures that have been manually categorized as noise. The decision-making process with the model is decoded by the classic activation map, which illuminates learning features of the DASEventNet model. These features provide clear illustrations of weak MEQs and varied noise types. Finally, we apply the trained model to the entire period (~7 days) of continuous DAS recordings and find that it discovers >5,700 new MEQs, previously unregistered in the public Silixa DAS catalog. The DASEventNet model significantly outperforms the traditional seismic method Short-Term Average/Long-Term Average (STA/LTA), which detected only 1,307 MEQs. The DASEventNet detection threshold is M_w−1.80 compared to the minimum magnitude of M_w−1.14 detected by STA/LTA. The spatiotemporal distribution of the newly identified MEQs defines an extensive stimulation zone and more accurately characterizes fracture geometry. Our results highlight the potential of DL for long-term, real-time microseismic monitoring that can improve enhanced geothermal systems and other activities that include subsurface hydraulic fracturing.

Plain Language Summary We introduce the DASEventNet model, a deep learning approach for detecting microearthquakes (MEQs) using distributed acoustic sensing (DAS) data. The model, based on a Residual Network Convolutional Neural Network (ResNet), is tailored to process large volumes of DAS data, a challenge for traditional methods. The model underwent rigorous validation processes, achieving an unprecedented 100% accuracy rate in distinguishing between 260 MEQs and noise raw test instances. Using a classic activation map, we highlighted the capacity of the model to differentiate between MEQs and varied noise types, even those bearing a resemblance to MEQs. The model could detect weak MEQs initially classified as noise, revealing its sensitivity. When applied to a week-long data set of DAS recordings, the model identified over 5,700 new MEQs, markedly surpassing the detection capabilities of the standard Short-Term Average/Long-Term Average (STA/LTA) approach and the initially cataloged ~1,307 MEQs. Notably, DASEventNet detects MEQs as low as M_w−1.80, more sensitive than the STA/LTA's M_w−1.14 threshold. The spatiotemporal analysis of these newly detected MEQs revealed a broader stimulation zone, offering a more precise delineation of fracture geometries. These findings underscore significant advantages of DASEventNet for long-term, real-time microseismic monitoring in enhanced geothermal systems and other subsurface activities.

1. Introduction

Enhanced geothermal systems (EGS) mark a significant advance in harnessing geothermal energy, particularly from impermeable Hot Dry Rock (HDR) formations. A critical component of EGS is hydraulic stimulation, a process designed to enhance rock permeability in HDR formations, thereby facilitating efficient heat exchange (Majer et al., 2007; Tester et al., 2006). This process, however, is inherently coupled with induced seismicity as

Project administration: Chris Marone, Derek Elsworth
Software: Pengliang Yu, Mingzhao Yu
Supervision: Tieyuan Zhu, Chris Marone, Derek Elsworth
Validation: Pengliang Yu
Writing – original draft: Pengliang Yu
Writing – review & editing: Tieyuan Zhu, Chris Marone, Derek Elsworth

fracture networks are reactivated within the reservoir with related concerns of seismic hazard (Gaucher et al., 2015; Majer et al., 2007).

Microseismic monitoring, traditionally executed through surface and downhole geophone arrays, has been pivotal in delineating the dynamics of hydraulic fracturing processes (Grechka & Heigl, 2017; Kwiatek et al., 2014; Maxwell, 2014; Staněk et al., 2022). It serves as a cornerstone for hydraulic fracture characterization and stimulated reservoir volume evaluation, informing operational decisions and hazard assessments. Traditional seismic monitoring methods, primarily reliant on geophone arrays, have limitations in terms of spatial resolution and susceptibility to surface noise interference (Eisner et al., 2010; Lellouch et al., 2020). This is especially problematic in densely populated or urban areas where anthropogenic activities significantly contribute to seismic noise, thereby hindering the detection of smaller but crucial seismic events (Lv et al., 2023; Stork et al., 2020; Verdon et al., 2020). The introduction of Distributed acoustic sensing (DAS) technology (Hartog, 2017) has substantially enhanced microseismic monitoring capabilities in the energy industry. This innovative technology, leveraging fiber-optic cables as dense seismic sensor arrays, enables detailed and extensive sampling of seismic wavefields. The excellent spatial resolution offered by DAS is particularly advantageous in hydraulic fracturing and EGS development, where delineating the geometry and understanding the complex dynamics of fracture networks and mitigating associated seismic risks are paramount (Jin & Roy, 2017; Lellouch et al., 2019; Ugueto et al., 2019). DAS has the ability to provide continuous, high-resolution seismic data using extensive lengths of fiber and represents a marked improvement over traditional seismic monitoring methods, leading to successful detection and analysis of microseismic events (Farhadiroushan, 2019; Karrenbach et al., 2019; Webster et al., 2013) and source mechanisms (Baird et al., 2020; Vera Rodriguez & Wuestefeld, 2020).

The applications of DAS extend from seismic monitoring for injected CO_2 plumes (Daley et al., 2013) to hydraulic fracturing monitoring (Bakku, 2015; Verdon et al., 2020), geothermal monitoring (J. Ajo-Franklin et al., 2022; Lellouch et al., 2020, 2021; Yu et al., 2023), flow monitoring (Mateeva et al., 2014; Shen & Zhu, 2023), icequake monitoring (Hudson et al., 2021; Walter et al., 2020), traffic vehicle monitoring (Martin et al., 2018; T. Zhu et al., 2021), and earthquake monitoring (Lindsey et al., 2017), showcasing its remarkable versatility across various fields. Recent reviews cover this broad range of applications (Lindsey & Martin, 2021; Zhan, 2019). However, the adoption of DAS technology brings its own set of challenges. The sheer volume of data generated, routinely reaching terabytes daily, poses significant computational and data processing hurdles (Clarke et al., 2019; Ma et al., 2023). This high data volume, coupled with the critical need for timely data analysis to inform operational decisions in hydraulic fracturing, underscores the necessity for advanced and efficient data processing methods. Moreover, the variable signal-to-noise ratio (SNR) along the fiber complicates the extraction of precise seismic signals, rendering traditional detection methods like STA/LTA less effective (Ma et al., 2023; W. Zhu et al., 2023).

Machine learning (ML) and deep learning (DL) methods have become a promising approach to overcome challenges in processing DAS data. These advanced methods can effectively handle large volumes of DAS data, identifying important features that would be difficult to extract using traditional data processing techniques. Developments in DL, like convolutional neural networks (CNNs), have proved to be particularly effective in classifying and analyzing seismic data, offering better detection capabilities than conventional algorithms (Perol et al., 2018; Ross et al., 2018; W. Zhu & Beroza, 2019). The application of machine learning to detect microseismic events in DAS data generally follows methods similar to those applied for station or geophone data (Boitz & Shapiro, 2024; Chai et al., 2022; Consolvo & Thornton, 2020; Hernandez et al., 2022). One strategy in this domain is the generation of synthetic microseismic events (Mousavi & Beroza, 2023) through methods such as anisotropic forward modeling (Stork et al., 2020), or employing homogeneous elastic medium forward modeling (Binder & Chakraborty, 2020). The use of synthetic data is advantageous, particularly in augmenting the number of training examples, a necessity in scenarios where high-quality, labeled seismic data are scarce or difficult to acquire (Leong & Zhu, 2024). Further developments include the integration of synthetic data into CNN frameworks (Binder & Tura, 2020), as well as the use of CNN-based transformer models (Liu et al., 2022; Yang et al., 2023). An alternative approach uses conventional seismic signals and noise, captured by traditional broadband seismometers (Hernandez et al., 2022) or geophones (Boitz & Shapiro, 2024). Ma et al. (2023) and Mousavi and Beroza (2022) used data augmentation strategies to artificially generate more events with various SNRs for training. However, a significant challenge with these synthetic models is their often-limited complexity, which may not adequately reflect the diverse range of real-world seismic scenarios (Mousavi et al., 2024). In contrast, several studies have directly utilized raw DAS data to train ML and DL models. Examples include

training VGG (Huot et al., 2022; Lellouch et al., 2022; Ma et al., 2023), ADE-Net2 (Lv et al., 2023), and U-net models (W. Zhu et al., 2023). These approaches leverage raw DAS data, which contain a broader spectrum of seismic signatures and anomalies typical of real-world scenarios. Recent work by Zhu et al. (2023) introduced PhaseNet-DAS. They used a pre-trained PhaseNet model (W. Zhu & Beroza, 2019) to produce phase picks and earthquake detection on Long Valley and Ridgecrest DAS cables. Furthermore, the preprocessing of DAS data has evolved to enhance the effectiveness of ML models. Techniques such as bandpass filtering, median subtraction (e.g., Chien et al., 2023), and median filtering (e.g., Liu et al., 2022), together with the implementation of STA/LTA methods (e.g., Lv et al., 2023), are employed to refine the data before it is fed into the ML algorithms. This preprocessing serves to isolate relevant seismic signals and reduce noise, thereby improving the training process. Most methods have demonstrated relative success, yet often fall short of the accuracy achieved through manual labeling. An exception is the advanced CNN model proposed by Huot et al. (2022), which, leveraging the continuous wavelet transform technique, successfully identified low-amplitude events in DAS fibers that were overlooked in manual analysis. In addition, a U-Net CNN microseismic event detection network trained on DAS and geophone data developed by Boitz and Shapiro (2024) provided a complete event catalog down to magnitude $M_w \sim -1.6$ for the 2019 Utah FORGE stimulation. Despite progress, challenges persist in interpreting and elucidating the intricacies of current machine learning models. Crucial questions remain unanswered, particularly regarding the specific criteria these models use to discern seismic events from noise, the features they assimilate during training, and whether their detection principles align precisely with established human understanding.

In this study, we developed the DASEventNet model, employing a Residual Network (ResNet) CNN architecture, to detect microseismic events from a week-long continuous data set recorded by the Silixa DAS fiber during Utah FORGE (Frontier Observatory for Research in Geothermal Energy) Well 16A (78)-32 hydraulic stimulation in April 2022. The DASEventNet model was trained on 1,309 raw DAS events (Silixa LLC, 2022), identified via STA/LTA, alongside an equal number of diverse noise samples. The DASEventNet model achieves a perfect accuracy of 100% in discriminating MEQs from noise in the raw test data sets, featuring learned characteristics that align with expert knowledge. We then apply the trained model to the entire period of DAS recordings, and successfully discover 5,749 new MEQs not registered in the public catalog generated by the STA/LTA method. The detectable minimum magnitude of the DASEventNet model is analyzed and its capability showcased in detecting low-magnitude events and some events that were manually classified as noise. We develop a comprehensive MEQ catalog and use it to investigate the seismicity response to hydraulic stimulation activities and evaluate the stimulated reservoir volume during hydraulic stimulations at the Utah FORGE site.

2. Data Set Acquisition and Generation

2.1. DAS Data Acquisition

Utah FORGE is a pioneering field laboratory dedicated to the development, testing, and demonstration of technologies essential for the commercialization of EGS (Moore et al., 2020). It utilizes four vertical wells—56-32, 58-32, 78A-32, and 78B-32—for seismic monitoring and tool testing. Well 16A (78)-32 serves as the injection well and is deviated at an angle of 65° from vertical. In April 2022, a three-stage hydraulic fracturing treatment was conducted at the toe of this well. The objective was to create fracture systems that facilitate long-term water circulation and efficient heat transfer between the injection well and the production well 16B (78)-32, drilled in 2023 (McLennan et al., 2023).

For the microseismic monitoring of the stimulations, an array of deep borehole geophone sensors was deployed as the primary network in well 56-32, 58-32, and 78B-32 under the current maximum limit of 200°C (Figure 1). The fiber-optic cables are installed in metal tubes cemented behind the casing in wells 78A-32 (up to a depth of 975.4 m) and 78B-32 (up to 1,219.2 m) (McLennan et al., 2023). A Silixa DAS interrogator connecting with the fiber is used to record mciroseismic signals, with a channel spacing of 1 m, a gauge length of 10 m, and a sampling rate of 4 kHz. In this study, we used DAS array data that were recorded continuously in well 78B-32 from 16 April 2022, at 16:30 (UTC) to 24 April 2022, at 14:30 (UTC), coinciding with the entire period of the three-stage stimulation conducted on well 16A (78)-32. There were also two levels of analog geophone pairs deployed post stimulation for continuous long-term monitoring of reservoir microseismicity. The works of Dyer et al. (2021) and Rutledge et al. (2022) provide a comprehensive summary of the monitoring system deployed at Utah FORGE.

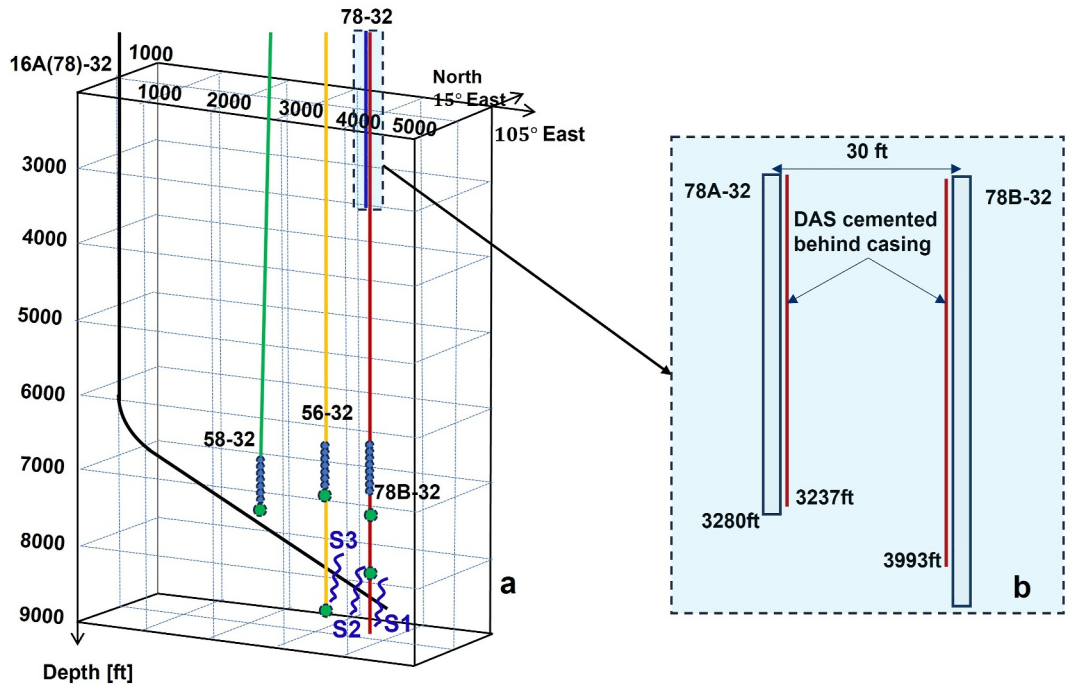

Figure 1. Perspective view of the hydraulic stimulation well 16A (78)-32, the three deep wells 58-32, 56-32, and 78B-32 and shallow well 78A-32 (reproduced from (Dyer et al., 2021; Rutledge et al., 2022)). Deep geophone chains in wells 56-32, 58-32, and 78B-32 are shown as blue dots, the depths of which were limited by temperature (<200°C). The analog geophone pairs, installed in the deep wells post stimulation, are shown as green dots. Silixa Distributed Acoustic Sensing fiber was installed behind the casing in wells 78A-32 and 78B-32 as shown in Figure 1b. The three stages of the stimulation experiments (S1, S2, S3) in well 16A (78)-32 are also shown in Figure 1a.

Silixa LLC provided a catalog of microseismic events recovered using an STA/LTA automatic event detection algorithm, complemented by bandpass filtering and signal-to-noise ratio (SNR) thresholding. This approach detected 1,309 events (Silixa LLC, 2022). However, the event location quality is poor due to the limitations of placement and completion depths of wells 78A-32 and 78B-32.

2.2. Data Set Generation

To develop an effective DL model for detecting microseismic events during hydraulic stimulation of well 16A (78)-32, we assembled a comprehensive data set comprising 1,296 events from the Silixa catalog, along with an equal number of noise examples. The original data set contained 1,309 events, but due to partial availability of Silixa DAS files, only 1,296 events were used for the analysis. The examples of noise were carefully selected from periods of DAS records when hydraulic stimulation activities were inactive, ensuring they were unlikely to contain overlooked low-amplitude events.

1. Data processing

To manage computational resources efficiently, we decimated the data to a sampling rate of 1 kHz. Each element in the data set was structured in a 2D data window, sized at 1,021 channels by 2,000 sampling points, corresponding to a 2-s duration. A band-pass filter ranging from 25 to 150 Hz was applied, informed by spectrogram analysis, to focus on the frequency range relevant to the microseismic events. Then we applied the median filter on the data to eliminate similar energy noise across channels.

2. Data labeling

The data set entries were labeled "1" for events (containing a single microseismic event) and "0" for noise. Rigorous manual checks were conducted on all 1,296 events to prevent mislabeling. A similar verification process was employed for noise samples, ensuring that they were accurately categorized and did not inadvertently contain microseismic energy. To enrich the model learning capability for microseismic detection, three different types of

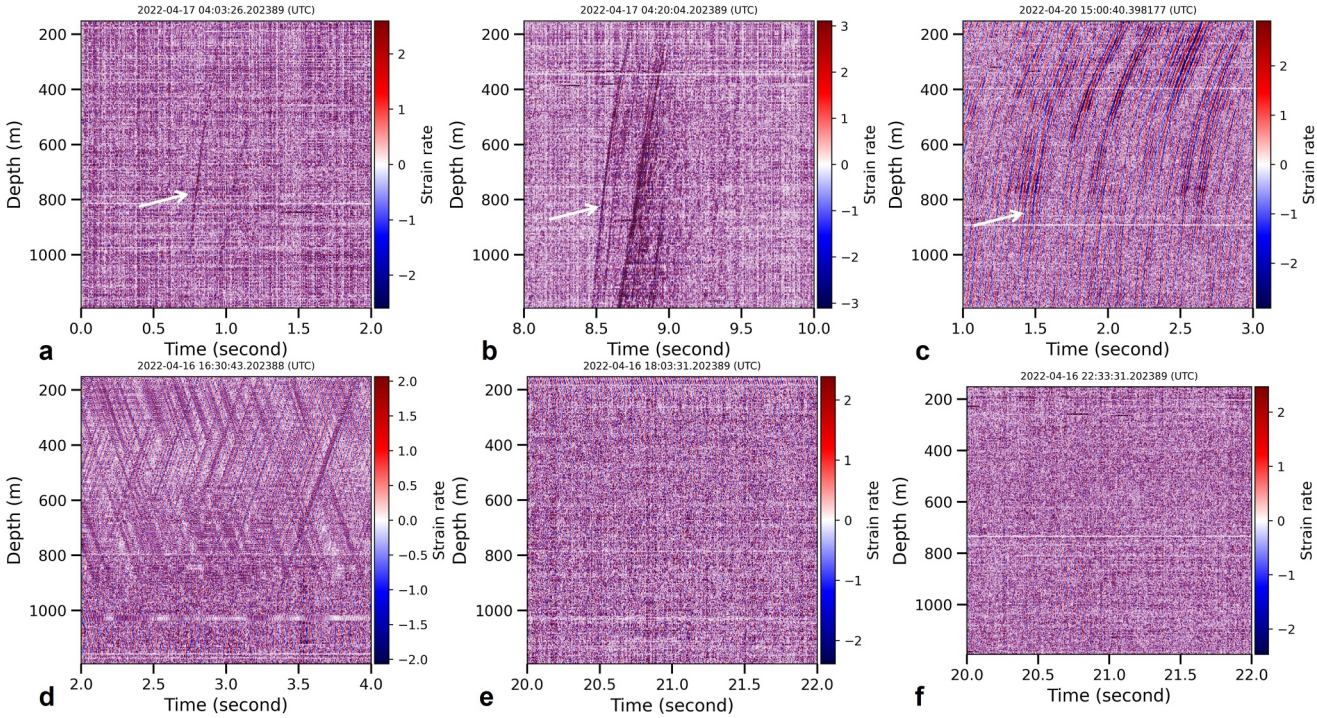

Figure 2. Examples of processed 2D data for deep learning model training. Panels (a–c) are three examples of microseismic events, displaying different levels of signal intensity to represent the range of events. Panels (d–f) illustrate three distinct types of noise encountered in the data set: (d) Type I noise, characterized by the tube-wave pattern; (e) Type II noise, marked by noticeable disturbances in the upper distributed acoustic sensing channels; and (f) Type III noise, random noise distinguished by its lack of regular or discernible pattern.

noise examples were included. Examples of the processed data windows, utilized as input for the DL model, are illustrated in Figure 2.

The data set was divided into training, validation, and test sets, maintaining a ratio of 0.75:0.15:0.1. Importantly, a balance between event and noise examples was maintained in each subset to ensure the effectiveness of the model across varying data types. Table 1 provides details of events and noise for each subset.

3. Deep Learning Model

Here, we treat the DL task as a binary classification problem, distinguishing between microseismic events and noise. The ResNet-50 architecture is employed in the DASEventNet model for its ability to train very deep neural networks. The key to its effectiveness lies in its skip-connections, which enable the network to avoid the vanishing gradient problem by reusing activations from previous layers. These residual connections are crucial for deep network training, ensuring that gradient information is not lost and that the training process continues effectively (He et al., 2016).

Table 1
Data Distribution Across Training, Validation, and Test Sets

Category	Training (75%)	Validation (15%)	Test (10%)	Total
Event (1)	969	193	130	1,292
Noise (0)	969	193	130	1,292
Total	1,938	386	260	2,584

3.1. Model Structure

ResNet-50, a deep CNN architecture comprising 50 layers, has revolutionized the field of computer vision and offers significant implications for geoscientific applications (Dramsch, 2020). It is composed of a stacked sequence of layers designed to facilitate the training of deep neural networks by leveraging residual learning, which addresses the degradation problem that occurs when networks become too deep.

The DASEventNet architecture, as illustrated in Figure 3, is structured into six main steps after the initial input layer. The initial step is characterized by a convolutional layer, which applies filters to the input to extract low-level

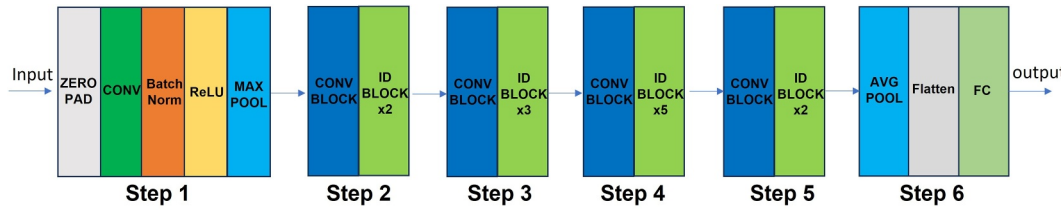

Figure 3. Schematic of the DASEventNet Architecture. This diagram illustrates the sequential steps of the DASEventNet model, beginning with the initial input followed by a zero-padding layer. The subsequent stages involve convolutional layers (CONV), batch normalization (Batch Norm), and activation functions (ReLU), concluding with a max pooling layer (MAX POOL). The core of the model consists of four steps with convolutional (CONV BLOCK) and identity blocks (ID BLOCK), where the ID BLOCK includes skip connections that bypass the intermediate layers, allowing the input to be added directly to the output. The final step transitions to classification with global average pooling (AVG POOL), flattening, and a fully connected (FC) layer (FC), leading to the output.

features. This is followed by batch normalization, which stabilizes the learning process by normalizing the output of the previous layer, and a ReLU activation function that introduces non-linearity to the model. A max pooling layer then reduces the spatial dimensionality, ensuring that the network remains computationally efficient.

The subsequent steps consist of a series of convolutional blocks (CONV blocks) and identity blocks (ID blocks), both of which contain layers of convolutional filters followed by batch normalization and ReLU activation. However, the convolutional blocks and the identity block serve different purposes within the network. A convolutional block typically serves as the starting block for each step after the first, and its role is to transform the feature maps both in terms of depth and spatial dimensions. Each convolutional block contains three layers of convolutions: the first 1×1 convolution reduces depth (number of filters), the 3×3 convolution operates at the reduced dimension to extract features, and the final 1×1 convolution restores the depth again. These layers are complemented by a shortcut connection that also modifies the dimensions to match the output, usually through a 1×1 convolution on the shortcut path.

In contrast, identity blocks do not alter the spatial dimensions or depth; they maintain the size of the input throughout. An identity block consists of similar layers of convolution blocks, but the shortcut connection simply adds the input directly to the output of the block without any transformation. This allows the network to focus on learning the residual mappings, effectively making the deeper layers refine the features extracted by previous layers without the risks of vanishing gradients.

In the final step, the network transitions from feature extraction to classification. It includes a global average pooling layer, which reduces each two-dimensional feature map to a single scalar, effectively summarizing the spatial information. This is followed by a flattening operation to convert the multidimensional tensors into a one-dimensional tensor, which is then fed into a fully connected (FC) layer that produces the model output.

3.2. Model Performance

We selected the DASEventNet model based on a specific set of parameters and callbacks to optimize training efficiency and classification accuracy. The training process was regulated by a learning rate scheduler starting with an initial rate of 1×10^{-4}. This rate was set to decrease by 50% after 10 epochs and 90% after 20 epochs, aligning with our strategy of fine-tuning the weights of networks during the training progression. The Adam optimizer (Kingma & Ba, 2015) was employed for its effectiveness in stochastic optimization, paired with binary cross-entropy (Zhang & Sabuncu, 2018) for the loss function, a standard choice for binary classification tasks. Accuracy was the chosen metric to evaluate model performance. To mitigate the risk of overfitting, an early stopping mechanism was integrated into the training process. This callback was configured to halt training if no significant improvement (greater than 1×10^{-4}) was observed in the validation loss over a span of 20 epochs. The model underwent extensive training with a batch size of 16 across 100 epochs, ensuring comprehensive learning and robust model performance without overfitting. Our best model achieved both 100% accuracy on the validation set with 386 samples and 100% accuracy on the un-touched test set including 260 samples as shown in Table 2.

Table 2
The DASEventNet Model Performance

Category		Accuracy (%)
Training set (1,938 samples)	969 events	100
	969 noises	
Validation set (386 samples)	193 events	100
	193 noises	
Test set (260 samples)	130 events	100
	130 noises	

To rigorously assess the performance and reliability of our optimal DASEventNet model, we conducted a comprehensive cross-validation procedure. This involved reshuffling the data set four additional times, each time redistributing the data (events and noises) into training, validation, and test sets for re-training. This method evaluated the model convergence and stability across different data splits, providing a robust measure of its generalizability.

Remarkably, in all five iterations, the model consistently achieved 100% accuracy in the validation set, successfully identifying MEQs from noise. On the test set, four iterations maintained 100% accuracy, while one iteration achieved 99.23% accuracy, with a minor discrepancy where two batches of noise were misclassified as events. These consistent results across multiple data configurations affirm the robustness and reliability of the model. Despite the slight variation in one test set iteration, the overall performance underscores the model effectiveness in accurately detecting MEQs.

3.3. Classic Activation Map

To elucidate the underlying features and patterns learned by our DASEventNet model and to understand its response to various inputs, we employed the technique of class activation mapping (CAM), a technique introduced by Zhou et al. (2016). This approach is able to visualize the activation patterns within final convolutional layers of the model, specifically after the global average pooling stage, as illustrated in Step 6 of the ResNet-50 architecture. Essentially, CAM lies in its ability to highlight the regions of the input image that are most influential in the model classification decision-making process.

As illustrated in Equation 1, the CAM is computed by aggregating the feature maps from the final convolutional layer of the ResNet50 model, each weighted by their corresponding coefficients from the FC layer. Specifically, this process involves multiplying each feature map by its associated weight — as determined in the FC layer — and then summing these products.

$$CAM = \sum_{i=1}^{n} w_i \times f_i \tag{1}$$

where f_i denotes the feature map output from the final convolutional layer, corresponding to the output of Step 5 in the ResNet50 model, as illustrated in Figure 3. The parameter w_i represents the weights associated with the FC layer of the ResNet50 model. Each neuron of the FC layer has a weight w_i which signifies the importance or contribution of a particular feature f_i toward the final classification decision.

Figure 4 presents the CAM examples of three events with varying strengths and complexity of seismic events as processed by the DASEventNet model. Those three events and/or coda in Figures 4a–4c are effectively highlighted by higher activation values in their distinct CAM plots (Figures 4d–4f). In contrast, as depicted in Figure 5, inputs representing three different types of noise exhibit lower activation values across the CAM plots (Figures 5d–5f). This difference between high activation values in Figure 4 and low activation values in Figure 5 indicates the effectiveness of our DASEventNet model for discriminating MEQs from noise. The alignment of the model detection criteria with human interpretation, as evidenced by these activation patterns, further attests to the robustness and reliability of the model in classifying MEQs.

3.4. Application of the Model to Entire DAS Records During the Well 16A (78)-32 Hydraulic Stimulation

We applied the DASEventNet model to the full data set (7-days) of continuous DAS recordings during the three-stage hydraulic stimulation. The data set extends from 17 April 2022, at 03:00 UTC to 23 April 2022, at 13:40 UTC and contains over 267,000 2D data windows. It took about 14.85 hr for the model to analyze the entire set of data windows, averaging 0.2 s to process each individual data window using 40 CPU cores at the Penn State Roar Collab cluster. The model identified 5,794 samples as microseismic events. We manually checked all predicted events, and only 45 events were false detections.

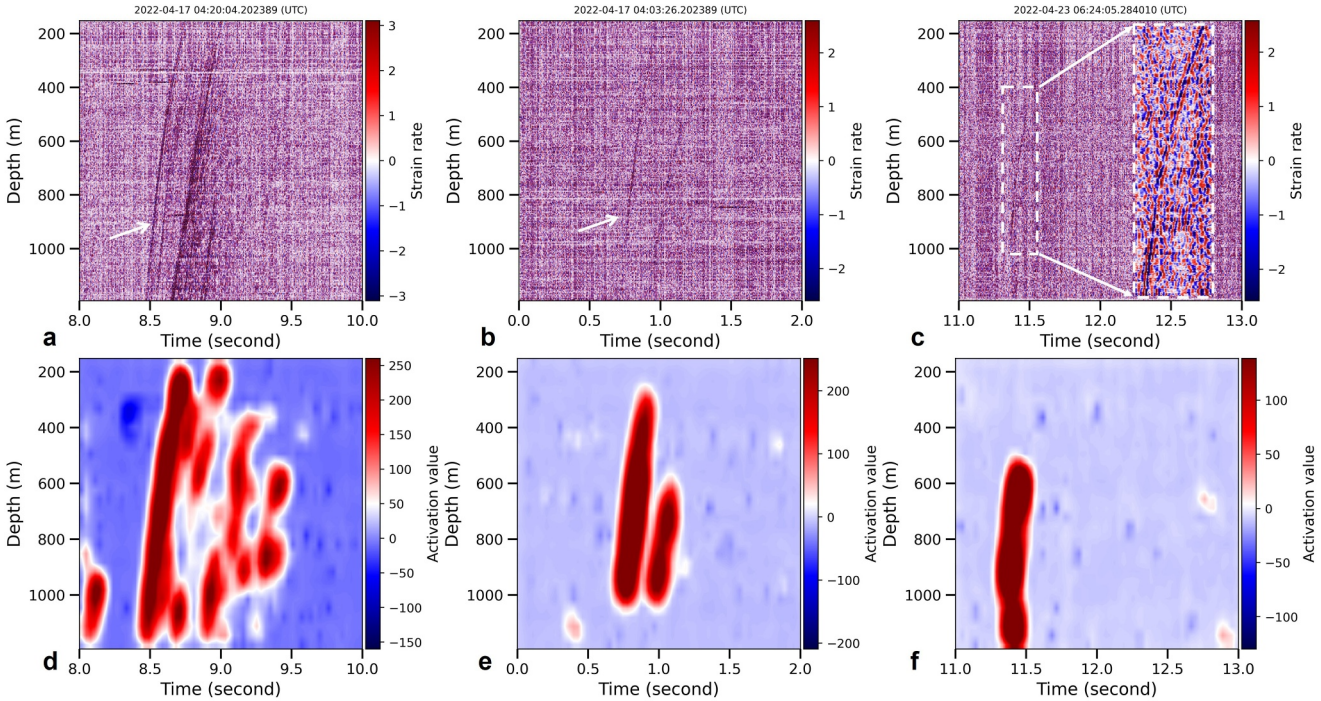

Figure 4. Comparative visualization of original event inputs and CAMs for the DASEventNet model. Panels (a–c) display three examples of input events processed by the model. Panels (d–f) correspond to their respective class activation mapping, which illuminate the regions within the inputs that are most influential in guiding the model classification decisions. Weak event signals are zoomed in and shown within the white frames for better visualization.

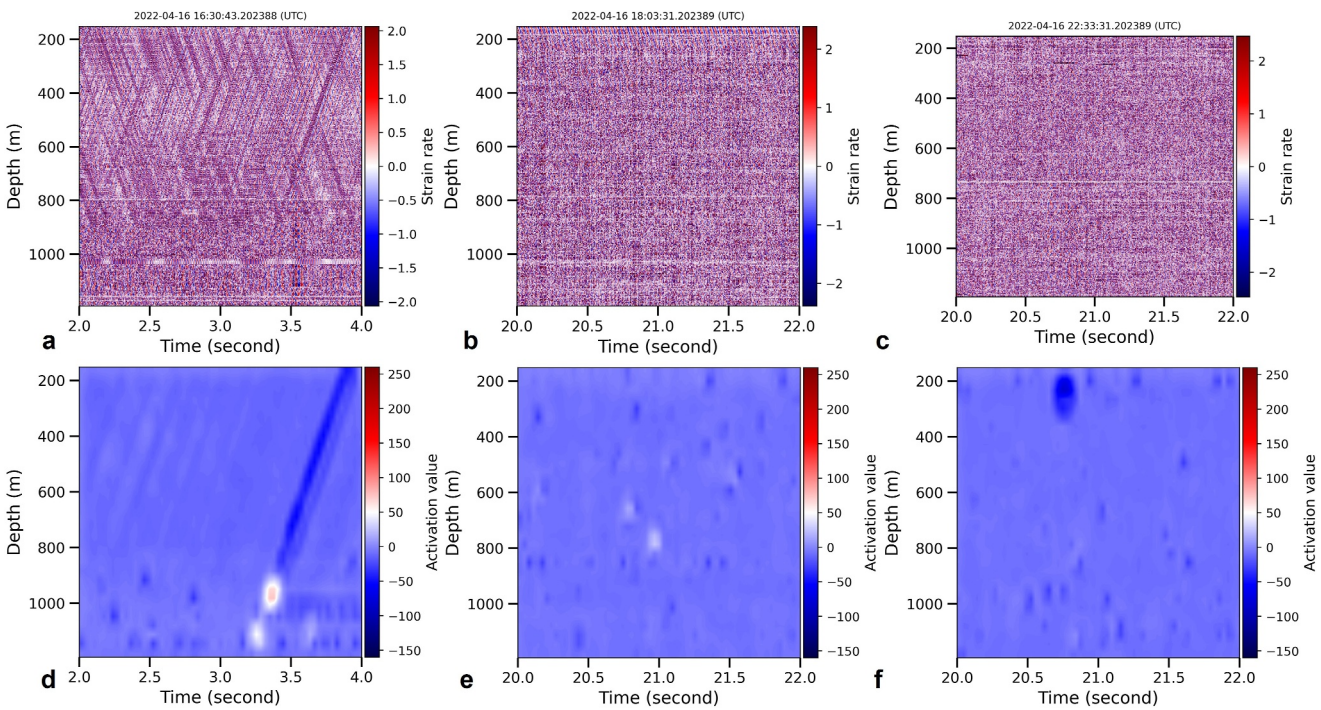

Figure 5. Comparative visualization of original noise inputs and CAMs for the DASEventNet model. Panels (a–c) display three examples of input noise packets processed by the model. Panels (d–f) correspond to their respective class activation mapping, which illuminate the regions within the inputs that are most influential in guiding the model classification decisions.

Table 3
Comparison of MEQs Detected in the Silixa Catalog, DASEventNet Model, the Catalog by Porras et al. (2023), and the Deep Borehole Geophone Catalog With Reliable Locations Introduced by Dyer et al. (2023) Across Different Stages

Stage	Silixa catalog (STA/LTA method)	Semblance-based seismic event detector (Porras et al., 2023)	DASEventNet	MEQs with reliable locations and magnitudes in deep borehole geophone catalog (Dyer et al., 2023)
1	45	/	227	823
2	57	/	309	1,323
3	1,207	2065	6,596	5,288
Total	1,309	/	7,132	7,434

Our method found 5,749 new MEQs that were not cataloged by Silixa using the traditional STA/LTA method, which detected 1,309 events. Thus our DL method expanded the catalog by a factor of ∼5. Table 3 presents a detailed comparison between the MEQs detected by the DASEventNet model and those identified by the STA/LTA method for each stage of well the 16A (78)-32 hydraulic stimulation. The total number of detected events, including those used for training the model, amounts to 226 in Stage 1, 289 in Stage 2, and 6,543 in Stage 3. This marks a significant improvement over the original STA/LTA method.

Porras et al. (2023) implemented a semblance-based seismic event detection method, analyzing the spatial coherence of seismic wavefields along geometrical hyperbolic trajectories in the 78B-32 well DAS data. They tested their method on the DAS data from the Stage 3 stimulation in well 16A (78)-32. They successfully identified 2065 reliable MEQs, doubling the number of events detected in Stage 3 using STA/LTA. In contrast, our model detected a total of 6,543 events in the Stage 3 stimulation, exceeding the event count detected by the method of Porras et al. (2023) more than threefold. Additionally, all the 2065 MEQs in the catalog provided by Porras et al. (2023) are detected by the DASEventnet model. Such an expansion demonstrates the superior performance and increased sensitivity of the developed model for detecting weak microseismic events in DAS data.

It is worth noting that Geo-Energie Suisse compiled a catalog of microseismic events (MEQs) during stimulations using deep borehole geophones deployed in wells 58-32, 56, and 78B. These wells are located much closer to the stimulation well 16A (78)-32 compared to the 78B-32 well used in this study (Figure 1). The deep borehole geophone catalog includes 36,641 MEQs, with 5,264, 6,732, and 24,645 events detected in Stages 1, 2, and 3, respectively (Dyer et al., 2023). However, as introduced by Dyer et al. (2023), only 823, 1,323, and 5,288 events in these stages have visually verified reliable locations and magnitude estimations. The rest of their detected events are problematic for their use. For instance, 14,502 events across the three stages were located using an unreliable automatic bootstrap method without verifications, and 14,705 events remained unlocated with unreliable magnitudes. For a detailed introduction to this deep borehole catalog, please refer to Supplementary Table S1 in Supporting Information S1. In this study, we only compared the MEQs with reliable location and magnitude data from the deep borehole geophone catalog by Dyer et al. (2023). As shown in Table 3, their catalog significantly increased the MEQ counts in Stages 1 and 2, while our model detected more events in Stage 3.

4. Discussion

4.1. Detection Capability of the ResNet Model

The detection capability of the DASEventNet model exceeds that produced by standard seismic techniques, but our procedure involves several steps. During manual inspection, some samples exhibited simultaneous presence of events and tube-wave noise within the same time window (Figures 6a and 6b). Figures 6c and 6d show their CAM plots, identifying a clear pattern of high activation values in the event signal zones, demonstrating the capability of the model to differentiate between event signals and tube-wave noise.

DASEventNet is designed for detecting MEQs from DAS data in the Utah FORGE project rather than estimating event locations and magnitudes. The challenges associated with estimating event magnitude using DAS amplitude information include issues such as unknown cable coupling, single-component sensing, uncertain instrumental response and uncommon amplitude saturation behaviors of DAS fibers (Ajo-Franklin et al., 2019; Lindsey et al., 2020), though some estimation methods were proposed (Gök et al., 2024; Lior, 2024; Yin et al., 2023).

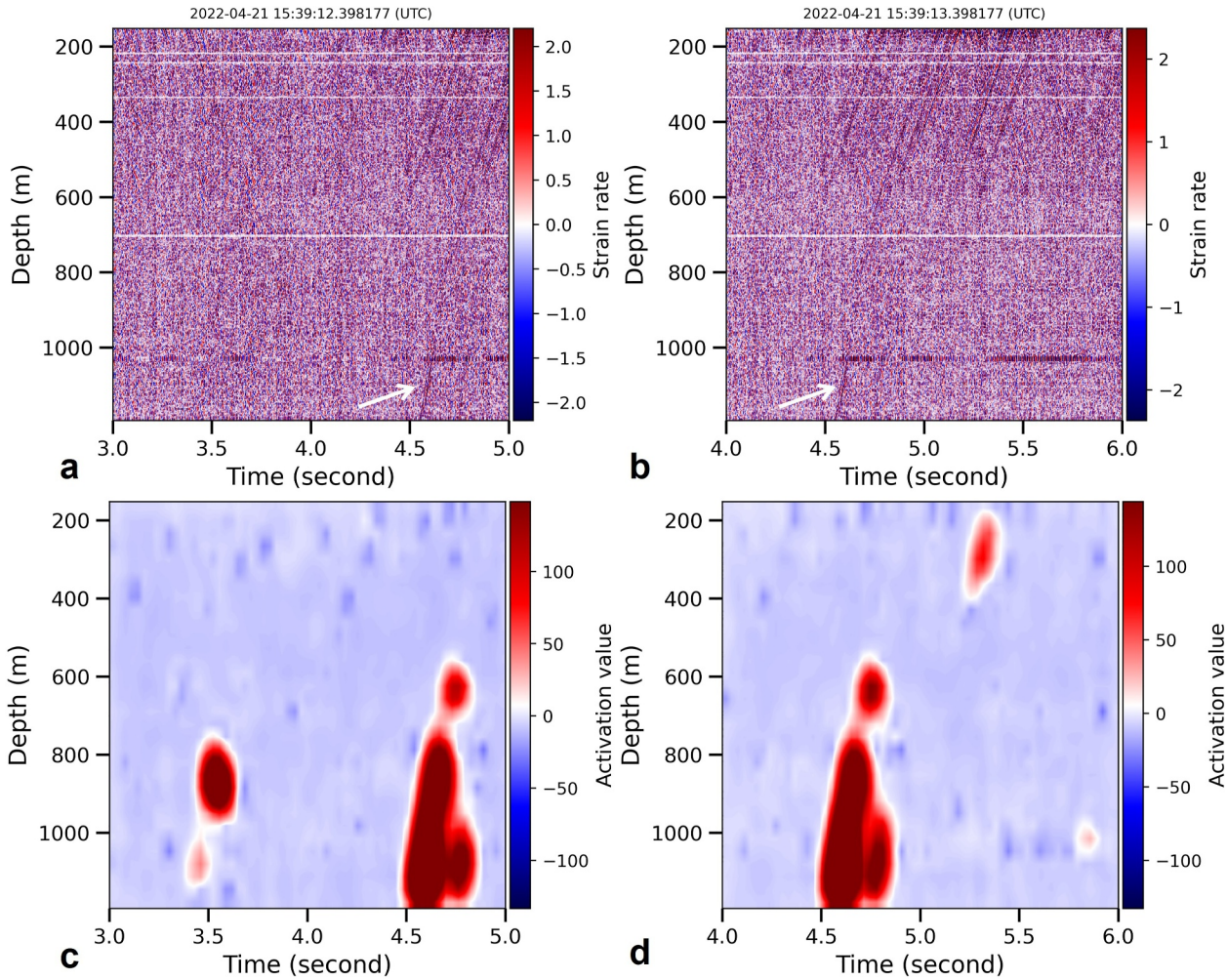

Figure 6. Data examples including both tube-wave noise and event signals (a–b), and their CAMs (c–d) for the DASEventNet model.

Additionally, direct determination of event locations from DAS recordings is also limited by the geometric placement and completion depth of the DAS fiber in well 78B-32.

Nevertheless, we also analyzed the minimum magnitude of events that could be detected by the DASEventNet model. We instead determine the DAS event magnitude and location by correlating event timings from the DAS with those recorded in the deep borehole geophone catalog provided by Geo-Energie Suisse. Due to different deployment depths of borehole geophones and DAS fibers (~1,000 m gap), a time discrepancy for the same events must exist but remains unknown. We used an ad-hoc timing match by assuming that if a DAS-recorded event occurred within a 0.2-s window after an event recorded in the deep borehole geophone catalog by Geo-Energie Suisse, they were considered the same event. The 0.2-s gap was determined by comparing the occurrence times of the same check shot event recorded in both the Geo-Energie Suisse geophone catalog and the Silixa DAS catalog. Similarly, reliable location information was derived using data from the deep borehole geophone catalog, given the challenges posed by the placement and completion depths of well 78B-32 in directly determining event locations from DAS fiber data.

With this event synchronization, we discovered that the DASEventNet model is capable of reliably detecting events with magnitudes as low as M_w−1.80 as shown in Figure 7b1. This detection capability is notably more sensitive than the minimum magnitude of M_w−1.14 (Figure 7a1) obtained using the traditional STA/LTA method used by Silixa LLC. In comparison, Boitz and Shapiro (2024) developed a U-Net CNN network for microseismic event detection in DAS data from the 2019 Utah FORGE stimulation. Their model, which incorporated the geophone information for training, could detect events magnitudes down to M_w−1.6. However, our

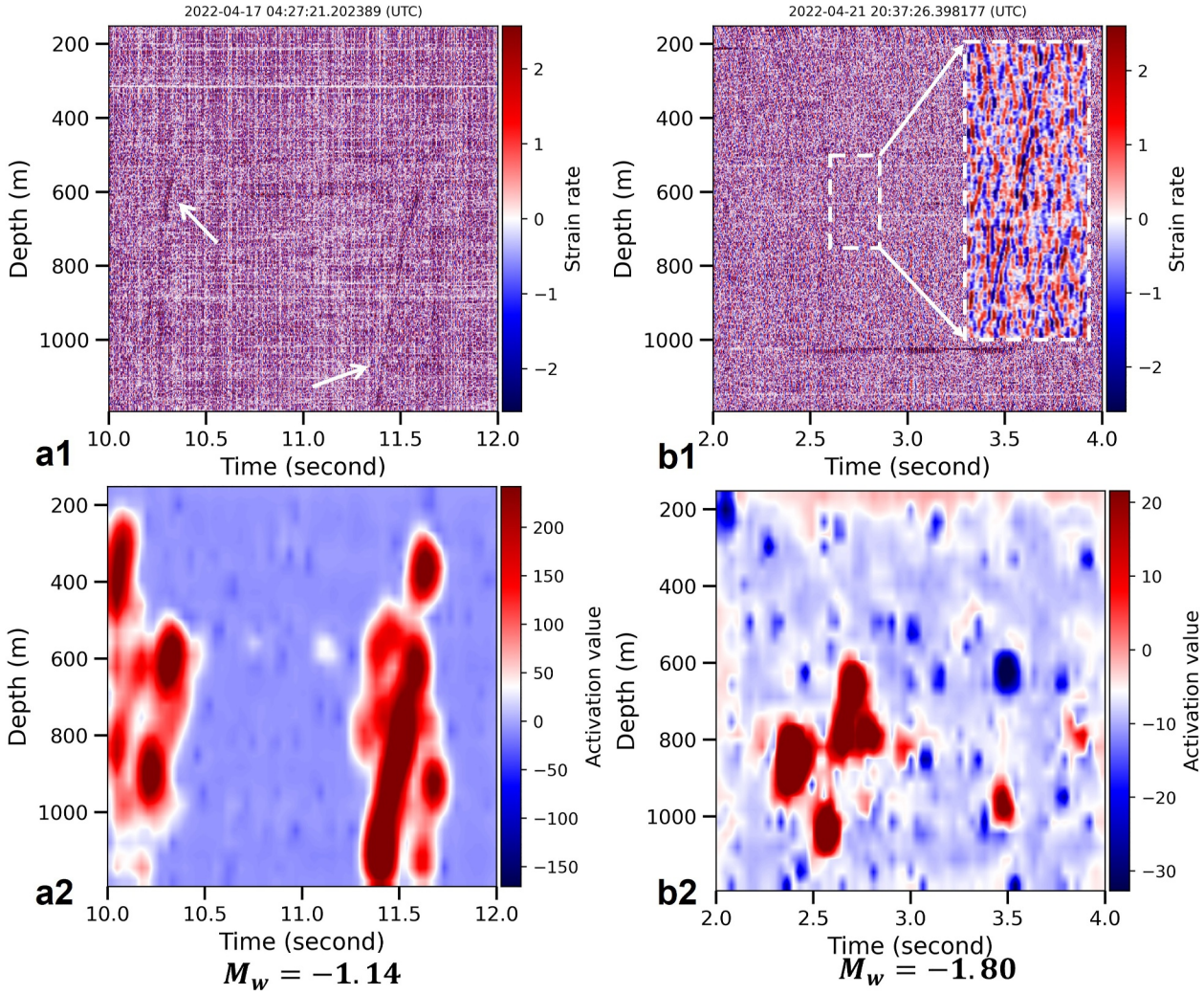

Figure 7. Comparison of minimum magnitude between events detected by the DASEventNet model and the STA/LTA Method. Panel (a1) shows the original distributed acoustic sensing (DAS) records with a magnitude of −1.14, the minimum event magnitude detectable by the STA/LTA method. Panel (b1) shows the original DAS records with a magnitude of −1.80, detectable solely by the proposed DASEventNet model. Panels (a2, b2) present the corresponding class activation mapping plots for panels (a1) and (b1), respectively. The weak event signals are zoomed in and shown within the white frames for better visualization.

DASEventNet model does not require geophone data for training and achieves a lower detectable magnitude compared to their approach. Figure 8 demonstrates a comparison of the magnitude distribution between events detected by our model and those identified by the STA/LTA method. The proposed DASEventNet detection model significantly increases the number of detected low-magnitude events across the three stages, indicating the superior capability of the model in identifying a broader range of seismic activities.

In addition, the model displayed an exceptional capability to identify unregistered weak events in the borehole geophone catalog that were not visually apparent in the original input data. The CAM plots for these events affirmed their classification, as shown in Figure 9. This outcome illustrates the comparable, and in some cases superior, performance of the model relative to manual classification methods, particularly in detecting weak events that might be missed in conventional visual analyses.

4.2. Spatiotemporal Distribution of MEQs During the Hydraulic Stimulation Period

The temporal evolution of microseismic events in response to injection and pressure histories in each stage of hydraulic stimulation was analyzed, as illustrated in Figure 10. Our developed model presented a more complete catalog for Stage 1 and Stage 2 stimulations compared to the Silixa catalog, leading to some interesting

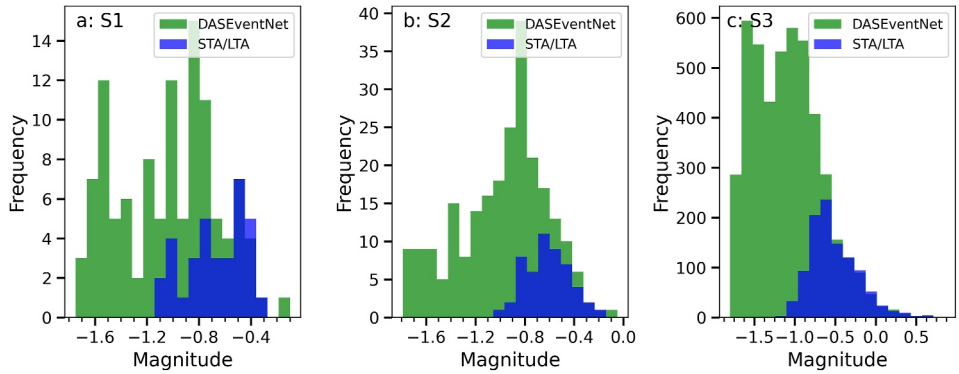

Figure 8. Comparison of microearthquakes (MEQs) magnitude distributions between catalogs detected by the developed DASEventNet model and STA/LTA method (Silixa LLC, 2022). Panels (a, b, c) are a comparison of the MEQ magnitude distribution for Stages 1, 2, and 3, respectively.

observations. For example, the peak seismicity rate (>8 events/minutes) in Stage 1 (Figure 10a) likely corresponds to rapid changes in injectivity over a short period, potentially due to transient poroelastic stresses in the reservoir that enhance earthquake triggering (Segall & Lu, 2015). The peak seismicity rate in Stage 2 (Figure 10b) might relate to well pressures reaching the formation breakdown pressure (~46.7 MPa) (McLennan et al., 2023) which then increases seismicity rate. Stage 2 also performed a hard shutdown midway through the maximum rate step (5.56 m^3/min) to examine the microseismic response and test the hypothesis that cyclic injection could reduce microseismicity (McLennan et al., 2023). However, no significant change in seismicity rate was observed before or after the hard shutdown from our catalog, as shown in Figure 10b, possibly due to the aforementioned limitations in SNR and large distances between the Stage 2 stimulation zone and the DAS fiber installation depth.

We also note that the temporal changes of detected events did not closely align with the entire injection and pressure history during these stages (Figures 10a and 10b). Several factors might contribute to this limitation.

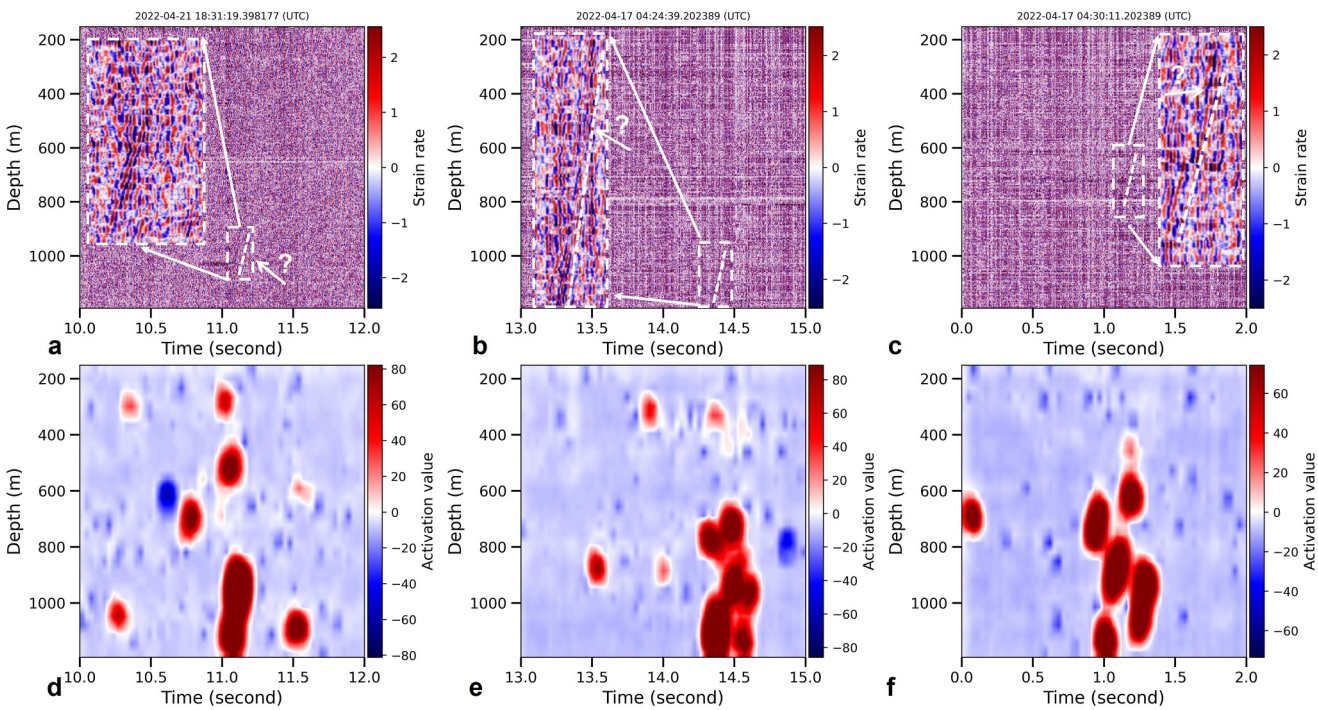

Figure 9. Comparative visualization of original inputs and their CAMs for the DASEventNet model. Panels (a–c) display three examples of inputs where event signals are not visually apparent. Panels (c–d) correspond to their respective CAMs with highlighted weak event signal regions. The weak event signals are zoomed in and shown within the white frames for better visualization.

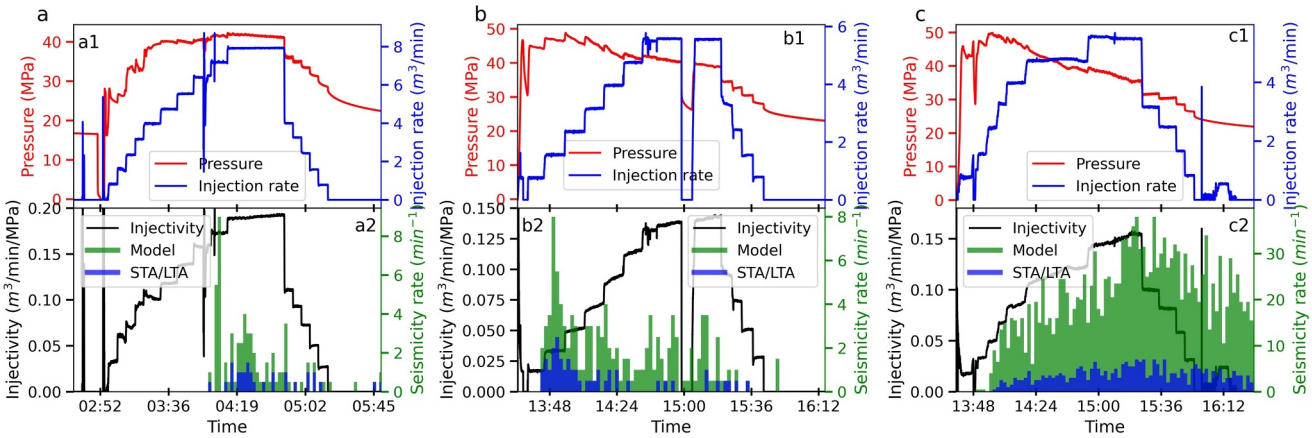

Figure 10. The three-stage stimulation history ((a): Stage 1, (b) Stage 2, (c) Stage 3) and corresponding microearthquakes sequences detected by the DASEventNet model and STA/LTA method (Silixa LLC, 2022). Panels (A1–C1) show the history of pressure and injection rate for Stage 1–3 stimulations. Panels (A2–C2) shows the injectivity (defined as the ratio between injection rate and pressure) together with the temporal evolution of seismicity as detected by our ResNet-50 model and STA/LTA methods, respectively during the three-stage stimulation.

From the perspective of DAS fiber detection capabilities, one possible reason is the well intervention activities during Stage 1 and Stage 2 in well 78B-32 (Silixa LLC, 2022), which resulted in a higher signal-to-noise-ratio (SNR) than Stage 3. For example, the average SNR values calculated for all 45 events in Stage 1 and the 57 events in Stage 2 in the Silixa LLC catalog had average SNR values of 2.80 and 2.67, respectively. However, the 1,208 events in Stage 3 had an average SNR of 3.27. Another factor is the different distances from stimulation zones of these three stages to the DAS fiber. As shown in Figure 1, Stage 1 and 2 stimulations were conducted at deeper locations in the 16A (78)-32 wellbore, with Stage 1 in a 200ft open-hole section at the wellbore toe (3,287.9m–3348.8 m measured depth (MD)) and Stage 2 in a 20ft perforation interval (3,218.7–3,224.8 m MD) (McLennan et al., 2023). In contrast, Stage 3 occurred in a 20 ft perforation interval at 3,084.6–3,090.7 m MD (McLennan et al., 2023). Given that the deepest channel of 78B-32 DAS fiber is installed at a depth of 1,037.2 m (Dyer et al., 2021), variations in stimulation depth could lead to significant differences in the seismic signal energy captured by the DAS fiber. Both Stages 1 and 2 pumped slickwater as the hydraulic fracturing fluid without proppant, whereas Stage 3 used crosslinked polymer fluid with microproppant (McLennan et al., 2023). The application of proppant could maintain hydraulic fractures open, and the stresses induced by tensile fracture opening plays a significant role in controlling the spatiotemporal evolution of induced seismicity (Kettlety et al., 2020). In addition, the lower response to injection history in Stage 1 might be due to the existence of multiple preexisting natural fractures in the openhole section (Xing, Damjanac, et al., 2022; Xing, Wray, et al., 2022; Zeinabady & Clarkson, 2023).

The temporal evolution of seismicity in Stage 3 demonstrated a more vigorous response to the injection history (Figure 10c). The seismicity rate increased with the increase in injectivity, peaking at maximum induced injectivity. Since MEQs are mechanistically linked to the creation of porosity and permeability (Fang et al., 2018; Ishibashi et al., 2018; Yu, Mali, et al., 2024, Yu, Zhu, et al., 2024), they are often used to evaluate the success of hydraulic stimulation (Riffault et al., 2018, 2019; Shapiro et al., 1997). The well-matched seismic response in Stage 3 may indicate successful creation of hydraulic fractures during stimulation. This could further be validated by the spatial distribution of the MEQs as shown in Figure 11, which illustrates the spatial distribution of MEQs as detected by the DASEventNet network and STA/LTA method. The quantification of stimulation zones in Stages 1 and 2, as indicated by the previous MEQ distributions in all catalogs, is not sufficient due to previously mentioned limitations. However, the Stage 3 MEQs detected by the proposed DASEventNet network revealed a more extensive stimulated reservoir volume. This suggests a more precise delineation of the fracture network created in the Stage 3 stimulation experiments in comparison to the MEQs detected by the STA/LTA method in the DAS arrays. In addition, the spatio-temporal distribution of the Stage 3 MEQs shown in Supplementary Figure S3 in Supporting Information S1 illustrates that the Stage 3 MEQs events migrate from the vicinity of the injection location to more distant locations and exhibit a planar fracture geometry perpendicular to the deviated wellbore. Despite significant differences in the locations of the monitoring wells, installation depths of geophones and DAS

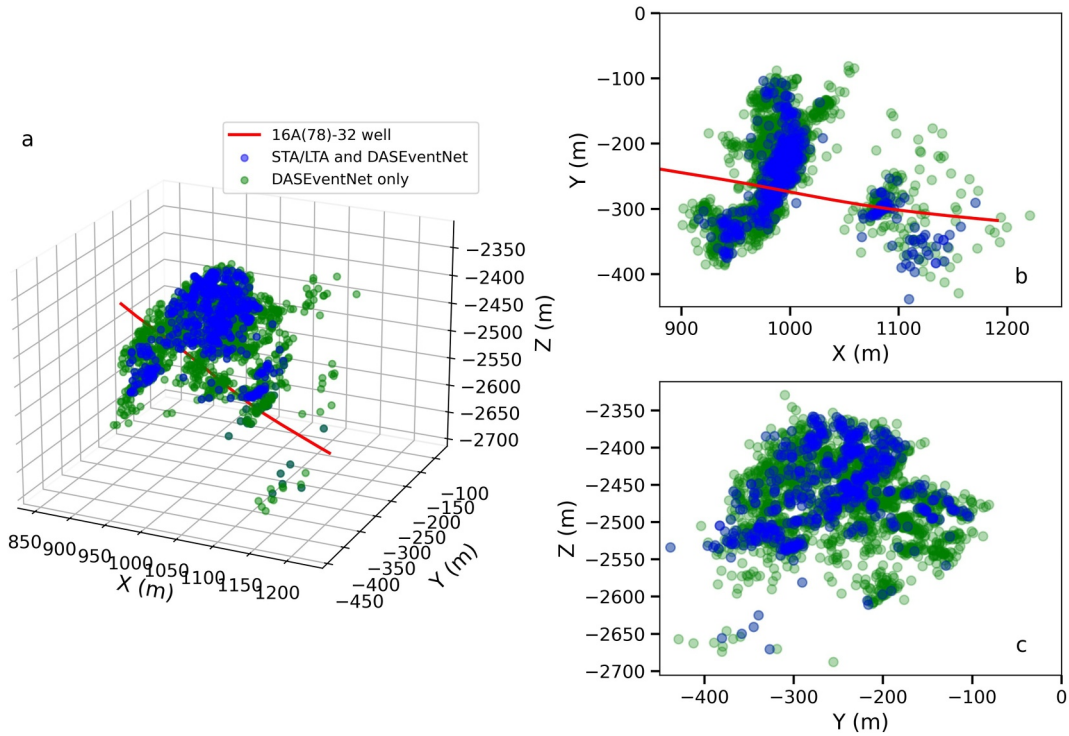

Figure 11. Comparison of microearthquake distributions between the DASEventNet model and the STA/LTA method. Events (in blue) detected by the STA/LTA method are also identifiable by the DASEventNet model. Panel (a) is the 3D distribution of microseismic events of the three stages detected by the DASEventNet model and the STA/LTA method. Panels (b) and (c) are the top view and side view of Panel (a) respectively.

fibers, and the sensitivity of geophones and DAS, we compared the Stage 3 MEQ distribution of DASEventNet to MEQs with reliable location in the deep borehole geophone catalog. As shown in Supplementary Figure S1 in Supporting Information S1, both catalogs exhibit similar fracture geometry in Stage 3.

5. Conclusions

We present a DL DASEventNet model for MEQ detection in continuous DAS data recorded during the hydraulic stimulation experiments in the Utah FORGE well 16A (78)-32 in April 2022. Our model was trained using catalog DAS events from well 78B-32, consisting of 1,292 MEQs and an equal number of noise samples. The model achieved a perfect accuracy of 100% in distinguishing MEQs from noise within the test data set containing 260 samples. We illustrated the learned features of the model on both event and noise samples by using the classic activation map technique. We found that the event signals were accurately captured and emphasized with higher activation values, while the noise domain exhibited lower negative activation values. This not only provides insights into how the model works but also ensures that detection criteria of the model are aligning with expert understanding. Notably, the activation maps revealed the capability of the model to detect weak MEQs that are manually classified as noise and to accurately capture the event signal domains where tube-wave noise is present.

We applied the DASEventNet model to the complete suite of DAS recordings for the entire hydraulic stimulation period, predicting a total of 7,058 MEQs. This number significantly surpasses the event count of 1,309 identified using the STA/LTA method, with the model revealing 5,749 new MEQs, which expanded the DAS catalog by ~5 times. Furthermore, the model exhibited a better detection capability compared to the semblance-based seismic event detection method introduced by Porras et al. (2023). In Stage 3 of the stimulation, the DL model detected 6,543 events, in contrast to the 2,065 MEQs identified by Porras et al. (2023). Compared to a detectable minimum magnitude of −1.14 based on the STA/LTA method, our ResNet-50 model demonstrates a remarkable capability in reliably detecting events with magnitudes as low as M_w−1.80. We observed that such minor events, typically elusive in conventional methods or manual classification, are effectively identifiable by the proposed DASEventNet model. The catalog compiled in this research reveals that the temporal evolution of seismicity rates in

Stage 3 exhibits a strong correlation with the injectivity history, suggesting a potential increase in permeability during stimulation. In addition, the spatial distribution of MEQs in Stage 3 indicates the successful creation of a stimulated volume of potentially reactivated fracture networks. These observations are particularly noteworthy despite the constraints posed by the fiber placement depths in well 78B-32. The MEQs detected by the DL model have significantly enhanced the understanding of the seismic response to the stimulation operation histories and fracture characterization in the hydraulic stimulations conducted in the Utah FORGE well 16A (78)-32 in April 2022.

The proposed model in this study holds potential for real-time and long-term monitoring of seismic events, not only during the stimulation experiments but also throughout the production period of EGS reservoirs. This capability is especially relevant where seismicity may be induced by the injection of cold water, demonstrating the versatility and applicability of the developed model in varied geothermal operation scenarios.

Data Availability Statement

The DAS data used in this study for the Utah FORGE well 16A (78)-32 stimulation can be found at Pankow (2022). The DAS catalog and report generated by Silixa LLC. for the Utah FORGE well 16A (78)-32 stimulation can be accessed via Silixa LLC (2022). The deep borehole geophone catalog can be accessed via: Karvounis et al. (2022). The DASEventNet model as well as the microseismic catalog are freely available at Yu et al. (2024a, 2024b).

Acknowledgments
We acknowledge support from the US Department of Energy under Grant DE-EE008763 and Grant EE0007080 through Utah FORGE. We thank Drs. Junzhu Shen and Zi Xian Leong for extensive helps on DAS data processing. TZ wants to thank AFRL Grant FA9453-21-2-0018 subawarded by Stanford University. CM acknowledges support from the European Research Council Advanced Grant 835012 (TECTONIC) and the RETURN Extended Partnership and funding from the European Union Next-GenerationEU National Recovery and Resilience Plan—NRRP, Mission 4, Component 2, Investment 1.3—D.D. 1,243 2/8/2022, PE0000005. DE gratefully acknowledges support from EGS-Collab funding through LBNL and the G. Albert Shoemaker endowment. The conclusions reported here are those of the authors. The authors thank the editor Dr. Rachel Abercrombie, the associate editor, Dr. Yuanyuan Ma, and an anonymous reviewer for their constructive reviews that significantly improved this manuscript.

References

Ajo-Franklin, J., Tribaldos, V. R., Nayak, A., Cheng, F., Mellors, R., Chi, B., et al. (2022). The Imperial Valley Dark Fiber Project: Toward Seismic Studies Using das and Telecom Infrastructure for Geothermal Applications. *Seismological Research Letters*, *93*(5), 2906–2919. https://doi.org/10.1785/0220220072

Ajo-Franklin, J. B., Dou, S., Lindsey, N. J., Monga, I., Tracy, C., Robertson, M., et al. (2019). Distributed acoustic sensing using dark fiber for near-surface characterization and broadband seismic event detection. *Scientific Reports*, *9*(1), 1–14. https://doi.org/10.1038/s41598-018-36675-8

Baird, A. F., Stork, A. L., Horne, S. A., Naldrett, G., Kendall, J. M., Wookey, J., et al. (2020). Characteristics of microseismic data recorded by distributed acoustic sensing systems in anisotropic media. *Geophysics*, *85*(4), KS139–KS147. https://doi.org/10.1190/geo2019-0776.1

Bakku, S. K. (2015). Fracture characterization from seismic measurements in a borehole. *PhD Thesis*. https://dspace.mit.edu/handle/1721.1/97331

Binder, G., & Chakraborty, D. (2020). Detecting microseismic events in downhole distributed acoustic sensing data using convolutional neural networks. *SEG International Exposition and Annual Meeting*, *2019*(1), 4864–4868. https://doi.org/10.1190/segam2019-3214863

Binder, G., & Tura, A. (2020). Convolutional neural networks for automated microseismic detection in downhole distributed acoustic sensing data and comparison to a surface geophone array. *Geophysical Prospecting*, *68*(9), 2770–2782. https://doi.org/10.1111/1365-2478.13027

Boitz, N., & Shapiro, S. (2024). Detection of microseismic events in continuous DAS data using convolutional neural networks. *The Leading Edge*, *43*(1), 16–22. https://doi.org/10.1190/TLE43010016.1

Chai, C., Maceira, M., & Team, E. G. S. C. (2022). Machine learning enhanced seismic monitoring at 100 km and 10 m scales. *47th Workshop on Geothermal Reservoir Engineering*, 635–645. http://energy.gov/downloads/doe-public-access-plan

Chien, C. C., Jenkins, W. F., Gerstoft, P., Zumberge, M., & Mellors, R. (2023). Automatic classification with an autoencoder of seismic signals on a distributed acoustic sensing cable. *Computers and Geotechnics*, *155*, 105223. https://doi.org/10.1016/j.compgeo.2022.105223

Clarke, H., Verdon, J. P., Kettlety, T., Baird, A. F., & Kendall, J. M. (2019). Real-time imaging, forecasting, and management of human-induced seismicity at preston new road, Lancashire, England. *Seismological Research Letters*, *90*(5), 1902–1915. https://doi.org/10.1785/0220190110

Consolvo, B., & Thornton, M. (2020). Microseismic event or noise: Automatic classification with convolutional neural networks. *SEG Technical Program Expanded Abstracts*, 1616–1620. https://doi.org/10.1190/segam2020-3414896.1

Daley, T. M., Freifeld, B. M., Ajo-Franklin, J., Dou, S., Pevzner, R., Shulakova, V., et al. (2013). Field testing of fiber-optic distributed acoustic sensing (DAS) for subsurface seismic monitoring. *The Leading Edge*, *32*(6), 699–706. https://doi.org/10.1190/tle32060699.1

Dramsch, J. S. (2020). 70 years of machine learning in geoscience in review. In *Advances in geophysics* (Vol. 61, pp. 1–55). Elsevier. https://doi.org/10.1016/bs.agph.2020.08.002

Dyer, B., Bethmann, F., Meier, P., Pankow, G. K., Wannamaker, P., Moore, J., et al. (2021). Microseismic monitoring and risk mitigation plan for the first Utah FORGE stimulations at the toe of 16A-32.

Dyer, B., Karvounis, D., & Bethmann, F. (2023). Microseismic event catalogues from the well 16A(78)-32 stimulation in April, 2022 in Utah FORGE. [Dataset]. https://gdr.openei.org/submissions/1558

Eisner, L., Hulsey, B. J., Duncan, P., Jurick, D., Werner, H., & Keller, W. (2010). Comparison of surface and borehole locations of induced seismicity. *Geophysical Prospecting*, *58*(5), 809–820. https://doi.org/10.1111/J.1365-2478.2010.00867.X

Fang, Y., Elsworth, D., & Cladouhos, T. T. (2018). Reservoir permeability mapping using microearthquake data. *Geothermics*, *72*, 83–100. https://doi.org/10.1016/j.geothermics.2017.10.019

Farhadiroushan, M. (2019). Seismic and microseismic detection using a wide dynamic-range distributed an engineered fiber optic acoustic sensor. *cp-556-00043*. https://doi.org/10.3997/2214-4609.201801921

Gaucher, E., Schoenball, M., Heidbach, O., Zang, A., Fokker, P. A., Van Wees, J. D., & Kohl, T. (2015). Induced seismicity in geothermal reservoirs: A review of forecasting approaches. In *Renewable and sustainable energy reviews*, (Vol. 52, pp. 1473–1490). Pergamon. https://doi.org/10.1016/j.rser.2015.08.026

Gök, R., Walter, W. R., Barno, J., Downie, C., Mellors, R. J., Mayeda, K., et al. (2024). Jonathan Ajo-Franklin; reliable earthquake source parameters using distributed acoustic sensing data derived from coda envelopes. *Seismological Research Letters*, *95*(4), 2208–2220. https://doi.org/10.1785/0220230270

Grechka, V., & Heigl, W. M. (2017). Microseismic monitoring. In *Microseismic monitoring*. Society of Exploration Geophysicists. https://doi.org/10.1190/1.9781560803485

Hartog, A. H. (2017). An introduction to distributed optical fibre sensors. In *An introduction to distributed optical fibre sensors*. CRC Press. https://doi.org/10.1201/9781315119014

He, K., Zhang, X., Ren, S., & Sun, J. (2016). Deep residual learning for image recognition. *Proceedings of the IEEE Computer Society Conference on Computer Vision and Pattern Recognition, 2016-December*, 770–778. https://doi.org/10.1109/CVPR.2016.90

Hernandez, P. D., Ramirez, J. A., & Soto, M. A. (2022). Deep-learning-based earthquake detection for fiber-optic distributed acoustic sensing. *Journal of Lightwave Technology*, *40*(8), 2639–2650. https://doi.org/10.1109/JLT.2021.3138724

Hudson, T. S., Baird, A. F., Kendall, J. M., Kufner, S. K., Brisbourne, A. M., Smith, A. M., et al. (2021). Distributed acoustic sensing (DAS) for natural microseismicity studies: A case study from Antarctica. *Journal of Geophysical Research: Solid Earth*, *126*(7), e2020JB021493. https://doi.org/10.1029/2020JB021493

Huot, F., Lellouch, A., Given, P., Luo, B., Clapp, R. G., Nemeth, T., et al. (2022). Detection and Characterization of Microseismic Events from Fiber-Optic das Data Using Deep Learning. *Seismological Research Letters*, *93*(5), 2543–2553. https://doi.org/10.1785/0220220037

Ishibashi, T., Elsworth, D., Fang, Y., Riviere, J., Madara, B., Asanuma, H., et al. (2018). Friction-stability-permeability evolution of a fracture in granite. *Water Resources Research*, *54*(12), 9901–9918. https://doi.org/10.1029/2018WR022598

Jin, G., & Roy, B. (2017). Hydraulic-fracture geometry characterization using low-frequency DAS signal. *The Leading Edge*, *36*(12), 975–980. https://doi.org/10.1190/TLE36120975.1

Karrenbach, M., Cole, S., Ridge, A., Boone, K., Kahn, D., Rich, J., et al. (2019). Fiber-optic distributed acoustic sensing of microseismicity, strain and temperature during hydraulic fracturing. *Geophysics*, *84*(1), D11–D23. https://doi.org/10.1190/geo2017-0396.1

Karvounis, D., Bethmann, F., & Dyer, B. (2002). Utah FORGE: Microseismic event catalogues from the well 16A(78)-32 stimulation in April, 2022. United States [Dataset]. https://gdr.openei.org/submissions/1558

Kettlety, T., Verdon, J. P., Werner, M. J., & Kendall, J. M. (2020). Stress transfer from opening hydraulic fractures controls the distribution of induced seismicity. *Journal of Geophysical Research: Solid Earth*, *125*(1), e2019JB018794. https://doi.org/10.1029/2019JB018794

Kingma, D. P., & Ba, J. L. (2015). Adam: A method for stochastic optimization. *3rd International Conference on Learning Representations, ICLR 2015 - Conference Track Proceedings*.

Kwiatek, G., Bulut, F., Bohnhoff, M., & Dresen, G. (2014). High-resolution analysis of seismicity induced at Berlín geothermal field, El Salvador. *Geothermics*, *52*, 98–111. https://doi.org/10.1016/J.GEOTHERMICS.2013.09.008

Lellouch, A., Horne, S., Meadows, M. A., Farris, S., Nemeth, T., & Biondi, B. (2019). DAS observations and modeling of perforation-induced guided waves in a shale reservoir. *The Leading Edge*, *38*(11), 858–864. https://doi.org/10.1190/tle38110858.1

Lellouch, A., Lindsey, N. J., Ellsworth, W. L., & Biondi, B. L. (2020). Comparison between distributed acoustic sensing and geophones: Downhole microseismic monitoring of the FORGE geothermal experiment. *Seismological Research Letters*, *91*(6), 3256–3268. https://doi.org/10.1785/0220200149

Lellouch, A., Luo, B., Huot, F., Clapp, R. G., Given, P., Biondi, E., et al. (2022). Microseismic analysis over a single horizontal das fiber using guided waves. *Geophysics*, *87*(3), 1–50. https://doi.org/10.1190/geo2021-0418.1

Lellouch, A., Schultz, R., Lindsey, N. J., Biondi, B. L., & Ellsworth, W. L. (2021). Low-magnitude seismicity with a downhole distributed acoustic sensing array—Examples from the FORGE geothermal experiment. *Journal of Geophysical Research: Solid Earth*, *126*(1). https://doi.org/10.1029/2020JB020462

Leong, Z. X., & Zhu, T. (2024). Microseismic monitoring using transfer learning: Example from the Newberry EGS. *Authorea Preprints*.

Lindsey, N. J., & Martin, E. R. (2021). Fiber-optic seismology. In *Annual review of earth and planetary sciences*, (Vol. 49(1), pp. 309–336). Annual Reviews. https://doi.org/10.1146/annurev-earth-072420-065213

Lindsey, N. J., Martin, E. R., Dreger, D. S., Freifeld, B., Cole, S., James, S. R., et al. (2017). Fiber-optic network observations of earthquake wavefields. *Geophysical Research Letters*, *44*(23), 11792–11799. https://doi.org/10.1002/2017GL075722

Lindsey, N. J., Rademacher, H., & Ajo-Franklin, J. B. (2020). On the broadband instrument response of fiber-optic DAS arrays. *Journal of Geophysical Research: Solid Earth*, *125*(2), e2019JB018145. https://doi.org/10.1029/2019JB018145

Lior, I. (2024). Accurate magnitude and stress drop using the spectral ratios method applied to distributed acoustic sensing. *Geophysical Research Letters*, *51*(1), e2023GL105153. https://doi.org/10.1029/2023GL105153

Liu, Y., Huff, O., Luo, B., Jin, G., & Simmons, J. (2022). Convolutional neural network-based classification of microseismic events originating in a stimulated reservoir from distributed acoustic sensing data. *Geophysical Prospecting*, *70*(5), 904–920. https://doi.org/10.1111/1365-2478.13199

Lv, H., Zeng, X., Chi, B., Zhang, G., & Thurber, C. (2023). Monitoring seismicity triggered by geothermal site shutdown with a surface DAS array at Brady Hot Springs. *Geophysical Journal International*, *235*(2), 1861–1871. https://doi.org/10.1093/GJI/GGAD333

Ma, Y., Eaton, D., Igonin, N., & Wang, C. (2023). Machine learning-assisted processing workflow for multi-fiber DAS microseismic data. *Frontiers in Earth Science*, *11*, 1096212. https://doi.org/10.3389/feart.2023.1096212

Majer, E. L., Baria, R., Stark, M., Oates, S., Bommer, J., Smith, B., & Asanuma, H. (2007). Induced seismicity associated with enhanced geothermal systems. *Geothermics*, *36*(3), 185–222. https://doi.org/10.1016/j.geothermics.2007.03.003

Martin, E. R., Huot, F., Ma, Y., Cieplicki, R., Cole, S., Karrenbach, M., & Biondi, B. L. (2018). A seismic shift in scalable acquisition demands new processing: Fiber-optic seismic signal retrieval in urban areas with unsupervised learning for coherent noise removal. *IEEE Signal Processing Magazine*, *35*(2), 31–40. https://doi.org/10.1109/MSP.2017.2783381

Mateeva, A., Lopez, J., Potters, H., Mestayer, J., Cox, B., Kiyashchenko, D., et al. (2014). Distributed acoustic sensing for reservoir monitoring with vertical seismic profiling. *Geophysical Prospecting*, *62*(4), 679–692. https://doi.org/10.1111/1365-2478.12116

Maxwell, S. (2014). Microseismic imaging of hydraulic fracturing. In *Microseismic imaging of hydraulic fracturing*. Society of Exploration Geophysicists. https://doi.org/10.1190/1.9781560803164

McLennan, J., England, K., Rose, P., Moore, J., & Barker, B. (2023). Stimulation of a high-temperature granitic reservoir at the Utah FORGE site. *Society of Petroleum Engineers - SPE Hydraulic Fracturing Technology Conference and Exhibition 2023, HFTC 2023*. https://doi.org/10.2118/212346-MS

Moore, J., Mclennan, J., Pankow, K., Simmons, S., Podgorney, R., Wannamaker, P., et al. (2020). The Utah frontier observatory for research in geothermal energy (FORGE): A laboratory for characterizing, creating and sustaining enhanced geothermal systems. *45th Workshop on Geothermal Reservoir Engineering*, 1–10.

Mousavi, S. M., & Beroza, G. C. (2022). Deep-learning seismology. *Science*, *377*(6607). https://doi.org/10.1126/science.abm4470

Mousavi, S. M., & Beroza, G. C. (2023). Machine learning in earthquake seismology. In *Annual review of earth and planetary sciences*, (Vol. 51(1), pp. 105–129). Annual Reviews. https://doi.org/10.1146/annurev-earth-071822-100323

Mousavi, S. M., Beroza, G. C., Mukerji, T., & Rasht-Behesht, M. (2024). Applications of deep neural networks in exploration seismology: A technical survey. *Geophysics*, *89*(1), WA95–WA115. https://doi.org/10.1190/GEO2023-0063.1

Pankow, K. (2022). Utah FORGE DAS seismic data [Dataset]. https://gdr.openei.org/submissions/1393

Perol, T., Gharbi, M., & Denolle, M. (2018). Convolutional neural network for earthquake detection and location. *Science Advances*, *4*(2). https://doi.org/10.1126/sciadv.1700578

Porras, J., Pecci, D., Bocchini, G. M., Gaviano, S., De Solda, M., Tuinstra, K., et al. (2023). A semblance-based microseismic event detector for DAS data. *Geophysical Journal International*, *236*(3), 1716–1727. https://doi.org/10.1093/gji/ggae016

Riffault, J., Dempsey, D., & Archer, R. (2019). Microearthquake enhanced permeability imaging of a stimulated well. *53rd U.S. Rock Mechanics/Geomechanics Symposium*. http://onepetro.org/ARMAUSRMS/proceedings-pdf/ARMA19/All-ARMA19/ARMA-2019-0106/1125832/arma-2019-0106.pdf

Riffault, J., Dempsey, D., Karra, S., & Archer, R. (2018). Microseismicity cloud can Be substantially larger than the associated stimulated fracture volume: The case of the paralana enhanced geothermal system. *Journal of Geophysical Research: Solid Earth*, *123*(8), 6845–6870. https://doi.org/10.1029/2017JB015299

Ross, Z. E., Meier, M. A., Hauksson, E., & Heaton, T. H. (2018). Generalized seismic phase detection with deep learning. *Bulletin of the Seismological Society of America*, *108*(5), 2894–2901. https://doi.org/10.1785/0120180080

Rutledge, J., Dyer, B., Bethmann, F., Meier, P., Pankow, K., Wannamaker, P., & Moore, J. (2022). Downhole microseismic monitoring of injection stimulations at the Utah FORGE EGS Site. *56th U.S. Rock Mechanics/Geomechanics Symposium*. https://doi.org/10.56952/arma-2022-0582

Segall, P., & Lu, S. (2015). Injection-induced seismicity: Poroelastic and earthquake nucleation effects. *Journal of Geophysical Research: Solid Earth*, *120*(7), 5082–5103. https://doi.org/10.1002/2015JB012060

Shapiro, S. A., Huenges, E., & Borm, G. (1997). Estimating the crust permeability from fluid-injection-induced seismic emission at the KTB site. *Geophysical Journal International*, *131*(2), 15–23. https://doi.org/10.1111/j.1365-246X.1997.tb01215.x

Shen, J., & Zhu, T. (2023). DAS with telecommunication fibre-optic cable in urban areas can record storm-induced seismic noise. *Geophysical Journal International*, *235*(3), 2122–2136. https://doi.org/10.1093/GJI/GGAD352

Silixa LLC. (2022). GDR: Utah FORGE: Well 16A(78)-32 2022 stimulation Silixa microseismic report [Dataset]. https://gdr.openei.org/submissions/1423

Staněk, F., Jin, G., & Simmons, J. (2022). Fracture imaging using DAS-recorded microseismic events. *Frontiers in Earth Science*, *10*, 907749. https://doi.org/10.3389/FEART.2022.907749/BIBTEX

Stork, A. L., Baird, A. F., Horne, S. A., Naldrett, G., Lapins, S., Kendall, J. M., et al. (2020). Application of machine learning to microseismic event detection in distributed acoustic sensing data. *Geophysics*, *85*(5), KS149–KS160. https://doi.org/10.1190/geo2019-0774.1

Tester, J. W., Anderson, B. J., Batchelor, A. S., Blackwell, D. D., & DiPippo, R. (2006). *The future of geothermal energy - impact of enhanced geothermal systems (EGS) on the United States in the 21st century* (Vol. 358). MIT - Massachusetts Institute of Technology. Retrieved from http://www1.eere.energy.gov/geothermal/egs_technology.html

Ugueto, G. A., Todea, F., Daredia, T., Wojtaszek, M., Huckabee, P. T., Reynolds, A., et al. (2019). Can you feel the strain? DAS strain fronts for fracture geometry in the BC montney, groundbirch. In *Proceedings - SPE annual technical conference and exhibition, 2019-September*. https://doi.org/10.2118/195943-MS.195943.

Vera Rodriguez, I., & Wuestefeld, A. (2020). Strain microseismics: Radiation patterns, synthetics, and moment tensor resolvability with distributed acoustic sensing in isotropic media. *Geophysics*, *85*(3), KS101–KS114. https://doi.org/10.1190/geo2019-0373.1

Verdon, J. P., Horne, S. A., Clarke, A., Stork, A. L., Baird, A. F., & Kendall, J. M. (2020). Microseismic monitoring using a fiber-optic distributed acoustic sensor array. *Geophysics*, *85*(3), KS89–KS99. https://doi.org/10.1190/geo2019-0752.1

Walter, F., Gräff, D., Lindner, F., Paitz, P., Köpfli, M., Chmiel, M., & Fichtner, A. (2020). Distributed acoustic sensing of microseismic sources and wave propagation in glaciated terrain. *Nature Communications*, *11*(1), 1–10. https://doi.org/10.1038/s41467-020-15824-6

Webster, P., Wall, J., Perkins, C., & Molenaar, M. (2013). Micro-seismic detection using distributed acoustic sensing. *Society of Exploration Geophysicists International Exposition and 83rd Annual Meeting, SEG 2013: Expanding Geophysical Frontiers*, 2459–2463. https://doi.org/10.1190/segam2013-0182.1

Xing, P., Damjanac, B., Moore, J., & McLennan, J. (2022). Flowback test analyses at the Utah frontier observatory for research in geothermal energy (FORGE) site. *Rock Mechanics and Rock Engineering*, *55*(5), 3023–3040. https://doi.org/10.1007/s00603-021-02604-x

Xing, P., Wray, A., Ignacio, E., Arteaga, V., Finnila, A., Moore, J., et al. (2022). In-situ stresses and fractures inferred from image logs at Utah FORGE. *Proceedigns 47th Workshop on Geothermal Reservoir Engineering*, 1–8.

Yang, Y., Birnie, C., & Alkhalifah, T. (2023). Joint microseismic event detection and location based on a detection transformer. *84th EAGE Annual Conference & Exhibition*, *1–5*. https://doi.org/10.3997/2214-4609.202310096

Yin, J., Zhu, W., Li, J., Biondi, E., Miao, Y., Spica, Z. J., et al. (2023). Earthquake magnitude with DAS: A transferable data-based scaling relation. *Geophysical Research Letters*, *50*(10), e2023GL103045. https://doi.org/10.1029/2023GL103045

Yu, P., Mali, A., Velaga, T., Bi, A., Yu, J., Marone, C., et al. (2024). Crustal permeability generated through microearthquakes is constrained by seismic moment. *Nature Communications*, *15*(1), 2057. https://doi.org/10.1038/s41467-024-46238-3

Yu, P., Zhu, T., Elsworth, D., & Marone, C. (2024b). DASEventNet (1.0) [Software]. *Zenodo*. https://doi.org/10.5281/zenodo.12194424

Yu, P., Zhu, T., Shen, J., Leong, Z. X., Marone, C., & Elsworth, D. (2023). Microearthquake event detection using deep learning: Distributed acoustic sensing data from Utah FORGE. *AGU23*.

Zeinabady, D., & Clarkson, C. R. (2023). Reservoir and fracture characterization for enhanced geothermal systems: A case study using multi-fractured wells at the Utah frontier observatory for research in geothermal energy site. *SPE Journal*, *1*(01), 1–14. https://doi.org/10.2118/217438-pa

Zhan, Z. (2019). Distributed acoustic sensing turns fiber-optic cables into sensitive seismic antennas. *Seismological Research Letters*, *91*(1), 1–15. https://doi.org/10.1785/0220190112

Zhang, Z., & Sabuncu, M. R. (2018). Generalized cross entropy loss for training deep neural networks with noisy labels. *Advances in Neural Information Processing Systems*, 8778–8788. https://arxiv.org/abs/1805.07836v4

Zhou, B., Khosla, A., Lapedriza, A., Oliva, A., & Torralba, A. (2016). Learning deep features for discriminative localization. *Proceedings of the IEEE Computer Society Conference on Computer Vision and Pattern Recognition, 2016-December*, 2921–2929. https://doi.org/10.1109/CVPR.2016.319

Zhu, T., Shen, J., & Martin, E. R. (2021). Sensing Earth and environment dynamics by telecommunication fiber-optic sensors: An urban experiment in Pennsylvania, USA. *Solid Earth*, *12*(1), 219–235. https://doi.org/10.5194/SE-12-219-2021

Zhu, W., & Beroza, G. C. (2019). PhaseNet: A deep-neural-network-based seismic arrival-time picking method. *Geophysical Journal International*, *216*(1), 261–273. https://doi.org/10.1093/gji/ggy423

Zhu, W., Biondi, E., Li, J., Yin, J., Ross, Z. E., & Zhan, Z. (2023). Seismic arrival-time picking on distributed acoustic sensing data using semi-supervised learning. *Nature Communications*, *14*(1), 1–11. https://doi.org/10.1038/s41467-023-43355-3

References From the Supporting Information

Aki, K. (1965). Maximum likelihood estimate of b in the formula log N= a-bM and its confidence limits. *Bulletin of Earthquake Research Institute, Tokyo University*, *43*, 237–239.

Shi, Y., & Bolt, B. A. (1982). The standard error of the magnitude-frequency b value. *Bulletin of the Seismological Society of America*, *72*(5), 1677–1687. https://doi.org/10.1785/BSSA0720051677

Wiemer, S., & Wyss, M. (2002). Mapping spatial variability of the frequency-magnitude distribution of earthquakes. In *Advances in geophysics* (Vol. 45, pp. 259–V). Elsevier. https://doi.org/10.1016/s0065-2687(02)80007-3